The Astrophysical Journal, 841:110 (16pp), 2017 June 1 https://doi.org/10.3847/1538-4357/aa6d86

The Coldest Place in the Universe: Probing the Ultra-cold Outflow and Dusty Disk in the Boomerang Nebula

R. Sahai[1], W. H. T. Vlemmings[2], and L-Å. Nyman[3]
[1] Jet Propulsion Laboratory, MS 183-900, California Institute of Technology, Pasadena, CA 91109, USA; raghvendra.sahai@jpl.nasa.gov
[2] Department of Earth and Space Sciences, Chalmers University of Technology, Onsala Space Observatory, SE-43992 Onsala, Sweden
[3] Joint ALMA Observatory (JAO), Alonso de Cordova 3107, Vitacura, Santiago, Chile, and European Southern Observatory, Alonso de Cordova 3107, Vitacura, Santiago, Chile
Received 2016 December 16; revised 2017 February 17; accepted 2017 April 12; published 2017 May 31

Abstract

Our Cycle 0 ALMA observations confirmed that the Boomerang Nebula is the coldest known object in the universe, with a massive high-speed outflow that has cooled significantly below the cosmic background temperature. Our new CO 1–0 data reveal heretofore unseen distant regions of this ultra-cold outflow, out to $\gtrsim$120,000 au. We find that in the ultra-cold outflow, the mass-loss rate ($\dot{M}$) increases with radius, similar to its expansion velocity (V)—taking $V \propto r$, we find $\dot{M} \propto r^{0.9-2.2}$. The mass in the ultra-cold outflow is $\gtrsim$3.3 $M_{\odot}$, and the Boomerang's main-sequence progenitor mass is $\gtrsim$4 $M_{\odot}$. Our high angular resolution ($\sim$0.″3) CO $J = 3$–2 map shows the inner bipolar nebula's precise, highly collimated shape, and a dense central waist of size (FWHM) $\sim$1740 au $\times$ 275 au. The molecular gas and the dust as seen in scattered light via optical *Hubble Space Telescope* imaging show a detailed correspondence. The waist shows a compact core in thermal dust emission at 0.87–3.3 mm, which harbors (4–7) $\times$ 10^{-4} $M_{\odot}$ of very large ($\sim$millimeter-to-centimeter sized), cold ($\sim$20–30 K) grains. The central waist (assuming its outer regions to be expanding) and fast bipolar outflow have expansion ages of $\lesssim$1925 years and $\leqslant$1050 years: the "jet-lag" (i.e., torus age minus the fast-outflow age) in the Boomerang supports models in which the primary star interacts directly with a binary companion. We argue that this interaction resulted in a common-envelope configuration, while the Boomerang's primary was an RGB or early-AGB star, with the companion finally merging into the primary's core, and ejecting the primary's envelope that now forms the ultra-cold outflow.

Key words: binaries: close – circumstellar matter – planetary nebulae: individual (Boomerang Nebula) – polarization – stars: AGB and post-AGB – stars: mass-loss

1. Introduction

The Boomerang Nebula (Wegner & Glass 1979), is a bipolar pre-planetary Nebula (PPN). PPNe are generally believed to represent a short-lived ($\sim$1000 years) transition phase during which Asymptotic Giant Branch (AGB) stars and their round circumstellar envelopes (CSEs) evolve into pre-planetary and planetary nebulae (PNe) with a breathtaking variety of aspherical geometrical shapes and symmetries (e.g., Sahai et al. 2007, 2011). The Boomerang holds the distinction of being the (naturally occurring) coldest known object in the universe (Sahai & Nyman 1997: SN97). The Boomerang's very large mass-loss rate ($\sim$0.001 $M_{\odot}$ yr^{-1}) and low-luminosity ($300L_{\odot}$) are unprecedented, making it a key object for testing theoretical models (i) for mass-loss during post-main-sequence evolution (e.g., Winters et al. 2000; Woitke 2006), and (ii) for producing the dazzling variety of bipolar and multipolar morphologies seen in PNe (Balick & Frank 2002).

Single dish CO $J = 1$–0 observations showed an extended high-speed outflow in absorption against the microwave background, implying that the nebula has cooled to a temperature significantly below that of the cosmic background radiation ($T_{bb} = 2.7$ K) due to adiabatic expansion, but the structure of the outflow was not properly resolved due to the large beam-size (45″). SN97 modeled the objects as consisting of two nested spherically symmetric shells: a warm inner shell extending 2.″5–6″ with an expansion velocity of about 35 km s^{-1}, and an ultra-cold, extended outer shell extending 6″–33″, with a velocity of about 164 km s^{-1}.

We mapped the Boomerang with ALMA in Cycle 0 in the CO $J = 1$–0 and 2–1 lines using the compact configuration (i.e., with 4.″3 and 2.″2 resolution) to determine the morphologies of its molecular outflows and compare it with the optical images (Sahai et al. 2013: Setal13). We confirmed that the extended high-velocity envelope has ultra-cold temperatures below the CMB, and, though patchy, shows no systematic departures from a roughly round shape, and the observed angular sizes of the inner and outer outflows were in reasonable agreement with the SN97 model. The inner outflow was found to have an hourglass shape with a dense central waist. The waist shapes the illumination of the nebula as a whole and provides a natural explanation for the overall hourglass optical morphology. We discovered patchy emission around the ultra-cold outflow, as expected from eventual heating of the gas due to grain photoelectric heating. Continuum emission at 1.3 and 2.6 mm indicated the presence of a substantial mass of millimeter-sized grains in the central dense waist.

Here, we report the highest-angular molecular-line observations of this object with ALMA at 0.88 mm, new CO 1–0 data that recover all of the flux from the very extended ultra-cold outflow, and continuum observations spanning the 0.88–3.3 mm wavelength range that robustly constrain the propertes of the central dust source. A preliminary version of some of the observational results from these data was given in Sahai et al. (2015).

The plan of the paper is as follows. In Section 2, we describe the observational setups, and data reduction and calibration

Table 1
Log of Observations

Band	Lines	Freq[a] GHz	Width GHz	$\delta V/\delta \nu$[b]	Array	Beam $'' \times ''$, (PA)°	Date yyyy mm dd	Time[c] minutes
3	^{12}CO (1–0)	115.271	1.875	1.3	12 m	2.26 × 1.29, 70.7	2013 Dec 17	52
	...[d]	...	...	...	ACA	12.7 × 8.4, 84.6	2014 Mar 20/21	192
	...	...	...	...	TP	57.4 × 57.4	2015 Apr 25/26	160
	SO (2, 3–1, 2)	99.2999	2.0	47	12 m	2.38 × 1.81, −87.4	2013 Dec 01	72
	cont	85.01	...	31.25	...	2.60 × 1.97, −89.1[e]	...	...
	...	87.01	...	...	...	...	...	...
	...	97.01	...	...	...	...	...	...
	....	99.01	...	...	...	...	...	...
7	^{12}CO (3–2)	345.796	1.875	0.5	...	0.37 × 0.25, 34.4	2014 Jun 14/15	96
	^{13}CO (3–2)	330.588	...	...	...	0.37 × 0.27, 34.9	...	...
	cont	331.26	...	0.49	...	0.43 × 0.35, 42.4	...	...
	...	333.15	...	...	...	...	...	...
	...	343.35	...	...	...	...	...	...
	...	345.25	...	...	...	...	...	...

Notes.
[a] Line center frequency, or center frequency, for the continuum band.
[b] Velocity width (km s^{-1}) per channel for line, frequency width (MHz) per channel for continuum.
[c] Total observation time (includes on-source integration time and other overheads).
[d] "..." indicates "same as" above everywhere in the table.
[e] Beam parameters for continuum datacube combining four bands at 85.01, 87.01, 97.01, and 99.01 GHz, with center frequency $\nu = 92.02$ GHz.

procedures. In Section 3, we present our main observational results. These include the molecular-gas morphology and kinematics of the central bipolar nebula and its dense waist, and a comparison with archival *Hubble Space Telescope* (*HST*) imaging in polarized light (Section 3.1), the physical properties of the ultra-cold outflow (Section 3.2), the unexpected discovery of SO emission (Section 3.3), the presence of very large grains in the central waist (Section 3.4), and the nebular polarization properties (Section 3.5). In Section 4, we discuss the implications of important timescales in the Boomerang derived from our data for theoretical models for the formation of jets and torii in AGB and post-AGB objects. We argue that the extreme properties of the ultra-cold outflow imply that a common-envelope event produced the Boomerang Nebula. The main conclusions of our study are summarized in Section 5.

Although we have adopted a distance of $D = 1.5$ kpc for the Boomerang (as inferred by SN97) for most of our analysis in this paper, we discuss the distance uncertainty where relevant.

2. Observations

A summary of the continuum and spectral line observations of the Boomerang Nebula is given in Table 1. The continuum Band 3 and CO $J = 3$–2 Band 7 observations were taken using a single pointing centered on R.A. $= 12^{h}44^{m}45\overset{s}{.}978$ and $\delta = -54°31'13\overset{''}{.}043$. The ^{12}CO $J = 1$–0 Band 3 observations consisted of a seven-point mosaic with the ALMA 12 m array and a five-point mosaic using the Atacama Compact Array (ACA) centered on the same position. Additionally, on-the-fly (OTF) mapping observations, using three ALMA Total Power (TP) antennas and a total of 160 minutes, were taken. The 12 m array observations were completed on 2013 December 17, the ACA observations on 2014 March 20–21 and the TP observations on 2015 April 25–26. By combining the 12-m, ACA, and TP data, the observations are sensitive to emission on all scales, with baselines ranging up to 1280 m. Flux calibration was done using Callisto (12 m Band 3 spectral line observations), Mars (ACA and 12 m continuum Band 3 observations), and Titan (12 m Band 7 observations). Bandpass and gain calibrations were performed using the quasars J1037-2934 and J1112-5703 for the 12 m Band 3 spectral line observations, and J1107-449 and J1303-5540 for all other observations. The data were calibrated using the Common Astronomy Software Application (CASA 4.2) and the observatory provided scripts with only a few additional flagging commands. The Band 3 data of the 12 m and ACA observations were combined in the visibility plane and imaged using natural weighting and a Gaussian taper radius of 100 $k\lambda$. Subsequently, the TP image, also obtained using the provided script, was combined with the interferometric image using the CASA task *feather*. The resulting beam sizes and position angles are provided in Table 1.

In order to assess possible flux loss in the interferometric ^{12}CO $J = 3$–2 observations, we obtained a spectrum of the line on 2014 October 8 using the APEX telescope. The observations were done in beam-switching mode using the SHeFI-APEX2 receiver.

3. Results

3.1. The CO($J = 3$–2) and Optical Imaging

3.1.1. Spatio-kinematic Structure of the Lobes

$J = 3$–2 line of both ^{12}CO and ^{13}CO were observed with the 12 m array with an angular resolution of about $0\overset{''}{.}3$ (Table 1). Our CO $J = 3$–2 integrated-intensity image ($-21.5 < V_{\rm lsr}$ (km s^{-1}) < 7.0) shows the precise, highly collimated shape of an inner bipolar structure and a dense central waist, with unprecedented angular resolution ($0\overset{''}{.}4$ or 600 au; Figure 1(a)).

For the first time, we have adequate angular resolution at millimeter-wavelengths to enable detailed matching between the molecular-line structure of the lobes in a PPN to the structure seen in scattered light in the optical. A comparison of the CO $J = 3$–2 image with a 0.6 μm polarized-light image obtained using the ACS (Figure 1(b), Cracraft & Sparks 2007) confirms the common interpretation of these as expanding,

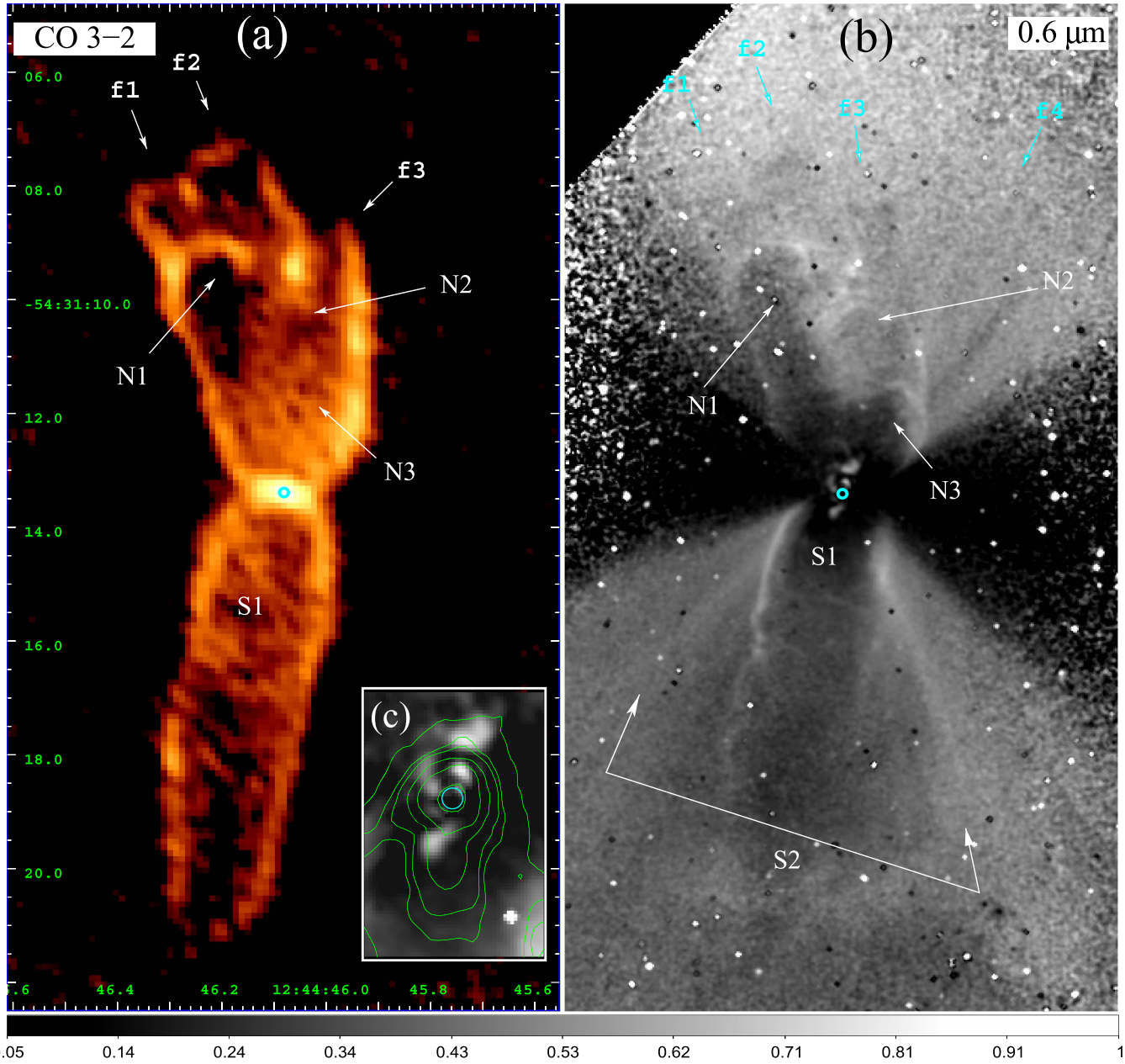

Figure 1. Central bipolar nebula in the Boomerang (a) ALMA ^{12}CO $J = 3$–2 moment zero map (integrated over the velocity range of $-21.5 < V_{\rm lsr}$ km s$^{-1} < 6.5$), and (b) *HST* image of the 0.6 μm percentage polarization. Inset (c) shows the expanded view of the central region $0\farcs65 \times 0\farcs95$ region, with contours showing the total 0.6 μm intensity at 0.47, 0.87, 1.1, 3.3, and 32%, of the peak. Cyan circles in the panels mark the location of the 0.87 μm continuum peak, at (J2000) R.A. = 12:44:46.084, decl. = −54:31:13.35.

thin-walled cavities. Since the absolute astrometry of the *HST* image is not sufficiently accurate, we have registered it relative to the ALMA images by forcing the 0.6 μm continuum peak to coincide with the 0.87 μm continuum peak.

Both the CO $J = 3$–2 and the optical images show that the N-lobe has a much more complex geometrical structure than the S-lobe. In the optical percentage polarized image, at least three limb-brightened, bubble-like structures can be clearly seen in the N-lobe (N1, N2, N3), and additional, much fainter structures can be seen beyond these (f1, f2, f3, and f4). In contrast, the S-lobe shows a single, bright cylindrical-shaped structure (S1), within a conical structure (S2). The N1, N2, and N3 bubbles merge together in one large limb-brightened structure in the CO $J = 3$–2 image. The f1 and f2 bubbles are seen much more clearly in the CO image than in the optical image. A more detailed discussion of the polarization in the Boomerang is provided in Section 3.5.

The channel maps of the $J = 3$–2 ^{12}CO and ^{13}CO emission are shown in Figures 2 and 3, and reveal the three-dimensional structure of the central bipolar nebula that was inferred from the lower angular-resolution $J = 2$–1 ^{12}CO map by Setal13. The ^{13}CO map shows a structure similar to that of ^{12}CO, but has a significantly lower S/N ratio, only the base and mid-latitude regions of the lobes are detected. The channels near the systemic velocity, $V_{\rm lsr} \sim -11.5$ km s^{-1} represent a cross-sectional cut through the lobes perpendicular to the line of sight (los). The

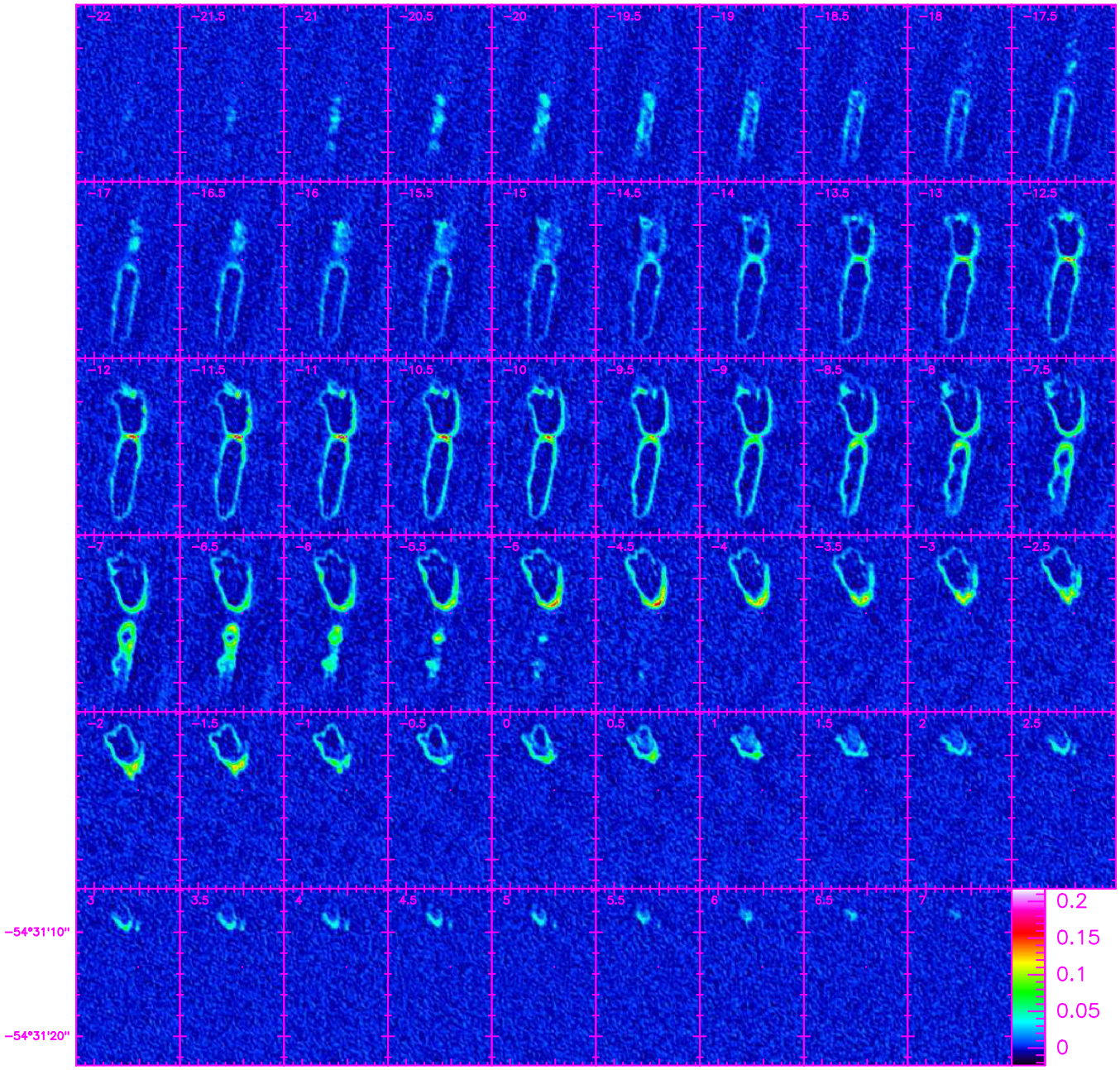

Figure 2. CO $J = 3$–2 channel map of the Boomerang. Intensity scale-bar units are Jy beam^{-1}. The 1σ noise is 4.8×10^{-3} Jy beam^{-1}.

spatial narrowing of the emission in the southern lobe (S-lobe) toward its axis as one approaches the blue- and redshifted channels ($V_{\rm lsr} \sim -20$ km s^{-1} and $V_{\rm lsr} \sim -6$ km s^{-1}) is expected because these channels sample material in the lobe walls that is moving directly toward or away from us.

As noted by Setal13, the lobes are not symmetrical—first, the S-lobe is much more elongated than the northern one (N-lobe), and second the symmetry axes of these lobes are not colinear. The N-lobe has a significantly more complex spatio-kinematic structure than the S-lobe, as also seen in the *HST* image. The N-lobe's axis is well-aligned with that of the S-lobe (at PA $\sim -8°$) in the blueshifted channels in the $V_{\rm lsr} \sim -17.5$ to -14.5 km s^{-1} range, and the progressive spatial narrowing of the emission toward the axis is similar to that seen for the southern lobe. However, in channels redward of $V_{\rm lsr} \sim -14.5$ km s^{-1}, the N-lobe's axis tilts progressively toward large PA values (29°), and is dominated by the change in orientation of its eastern wall. The western wall of the N-lobe is less affected in this manner, especially its low-latitude basal region toward the west, which corresponds to the western wall of the N3 optical lobe.

We derive an upper limit of 1050 years to the expansion timescale of the S-lobe by dividing its linear extent, $7\farcs9$ or 1.8×10^{17} cm, by the deprojected expansion velocity, $\geqslant 14$ km s^{-1}/sin(θ), where $90° > \theta \lesssim 75°$ is the lobe's inclination[4] (Setal15). The expansion timescale of the N-lobe is comparable or smaller, because its linear extent is somewhat smaller, but since its structure is significantly more complex, we cannot constrain it as well as for the S-lobe.

[4] All inclination angles, here and elsewhere in the paper, are relative to the los.

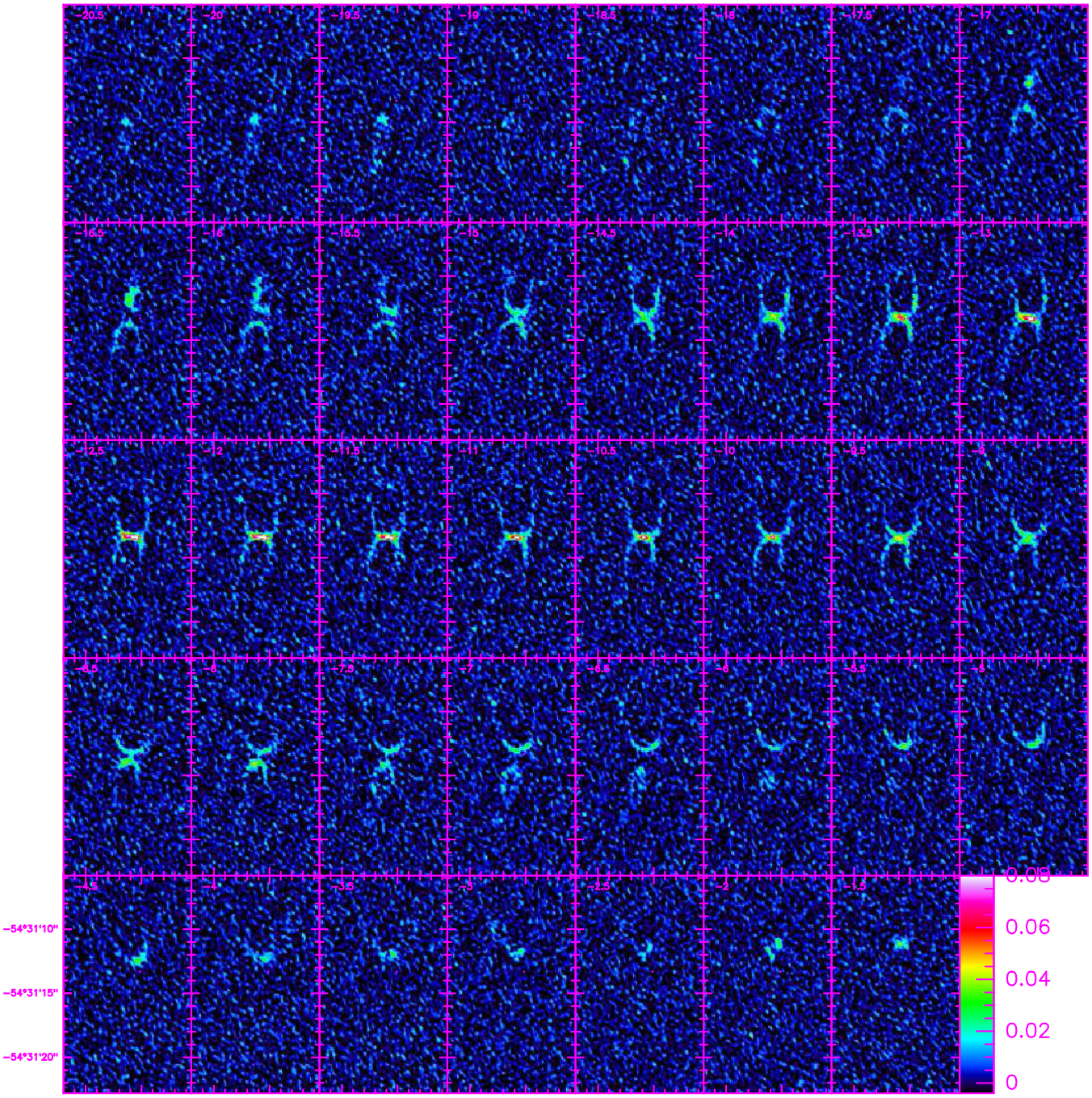

Figure 3. ^{13}CO $J = 3$–2 channel map of the Boomerang. Intensity scale-bar units are Jy beam^{-1}. The 1σ noise is 5.3×10^{-3} Jy beam^{-1}.

We obtained a single-dish spectrum of the CO $J = 3$–2 emission from the Boomerang with the 17.″8 beam of the 12 m APEX (Atacama Pathfinder EXperiment) telescope (Figure 5). The peak intensity is about 0.2 K, implying a total flux of about 8.2 Jy. The ALMA observations thus resolve out about 4 Jy of extended emission.

3.1.2. Spatio-kinematic Structure of the Waist

The central waist, which is seen nearly edge-on in the ^{12}CO and ^{13}CO $J = 3$–2 images (Figure 4), is geometrically thin. We measure a width (FWHM) along its minor axis of 0.″36 in the less optically thick ^{13}CO $J = 3$–2 line. Since the beam has an FWHM size 0.″37 × 0.″265 (PA = 34.°9) and is oriented at about 40° relative to the waist, the latter is at best, marginally resolved in a direction perpendicular to its plane, and has a deconvolved minor axis of $\lesssim$0.″18 ($\lesssim$275 au).

In spectra extracted from a 0.″3 × 0.″2 region in the waist-center as seen in the $J = 3$–2 ^{12}CO and ^{13}CO images, the velocity width (FWHM ~ 4.5 km s^{-1}) is significantly smaller than that in the bipolar outflow (Figures 6(a), (b)). A comparison of the waist $J = 3$–2 ^{12}CO line profile with that extracted from our lower angular-resolution $J = 2$–1 ^{12}CO data (Setal13, Figure 3(b)) spectrum shows a very signficant improvement in the isolation of the waist emission from the lobes. A position–velocity cut of the ^{13}CO $J = 3$–2 intensity taken along the major axis of the waist has a morphology that is not a simple ellipse (as expected for expansion), and possibly

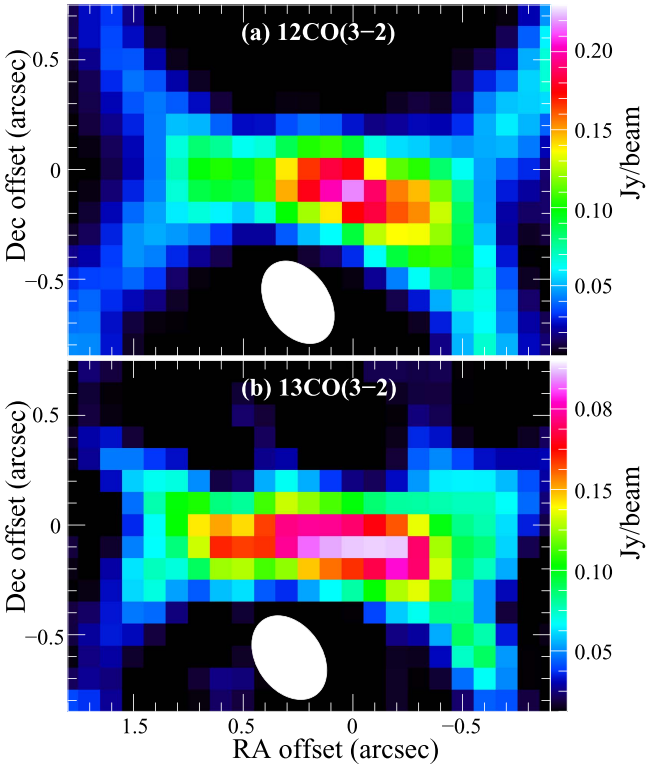

Figure 4. Waist of the Boomerang Nebula, as seen in (a) ^{12}CO $J = 3$–2 (white ellipse: beam FWHM 0.″37 × 0.″25, PA = 34.°4), and (b) ^{13}CO $J = 3$–2 (white ellipse: beam FWHM 0.″37 × 0.″26, PA = 34.°4) images, at the central velocity of the waist emission profile, $V_{\rm lsr} = -12$ km s^{-1}.

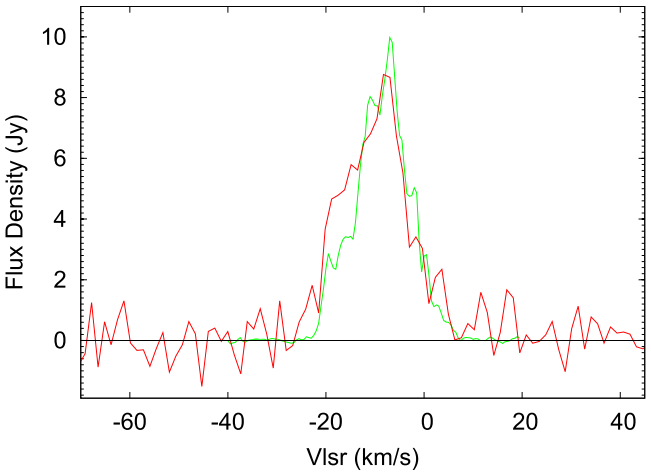

Figure 5. Single-dish (APEX) CO $J = 3$–2 spectrum of the Boomerang, compared to the spatially integrated ALMA spectrum (scaled up by a factor of two).

includes a component due to Keplerian rotation (Figure 6(c)). If true, then the central region of the Boomerang resembles the disk in the Red Rectangle and IW Car (dubbed disk-prominent post-AGB or dpAGB objects by Sahai et al. 2011), that show Keplerian rotation (expansion) in their inner (outer) regions (Bujarrabal et al. 2016, 2017). Higher angular-mapping with ALMA can easily test this possibility. We note that the velocity width of the Boomerang's waist is the smallest, compared to the velocity-widths of the central torii in a sample of PPNe compiled by Huggins (2012, 2007).

If some (or all) of the material in the Boomerang's waist lies in a rotating disk, we cannot determine its age. If the disk results from a prolonged binary interaction, i.e., not a common-envelope event (but see Section 4, where we argue that a common-envelope event is the most plausible scenario), then it is likely long-lived, like the disks in dpAGB objects, many of which have known central binary stars (de Ruyter et al. 2006; van Winckel et al. 2009; Bujarrabal et al. 2013). Assuming that outer regions of the Boomerang's waist are in expansion, we roughly estimate an expansion age of 1925 years, by dividing the half-power extent (deconvolved) of the ^{13}CO $J = 3$–2 waist emission (1.″16 or 1740 au) by its half-power velocity width (FWHM = 4.3 km s^{-1}). Because the waist emission is not very clearly isolated from that arising in and near the base of the lobes, it is likely that the waist size (age) is somewhat smaller than 1740 au (1925 years).

The centroid of the ^{13}CO line is blueshifted from that of the ^{12}CO line. This can be explained as the well-known radiative-transfer effect in an optically thick expanding medium where the excitation temperature falls with radius (and may also require a velocity gradient). The ^{12}CO and ^{13}CO line intensity ratio is quite low, implying that the ^{12}CO $J = 3$–2 is certainly optically thick. Simple modeling using RADEX (Van der Tak et al. 2007) suggest that the kinetic temperature is $\gtrsim$27 K, and N(CO) $\sim 10^{17}$ cm^{-2}, resulting in an optical depth of the ^{12}CO $J = 3$–2 line of, $\tau(3\text{–}2) = 2.4$. For $\tau(3\text{–}2)$ half this value, the model ^{12}CO $J = 3$–2 brightness temperature is 11.5 K, significantly lower than the observed 16 K. The number density $n(H2) \gtrsim$ few $\times 10^4$ cm^{-3} in order for excitation to be not subthermal. If the excitation is subthermal, then $T_{\rm kin}$ is greater than 27 K. For these parameters, the ^{13}CO/^{12}CO ratio is 1/3.3 (the maximum value attained during equilibrium CNO nucleosynthesis), and the ^{13}CO $J = 3$–2 optical depth is 0.5. Of course, if ^{12}CO $J = 3$–2 is more optically thick, the ^{13}CO/^{12}CO ratio will be lower. Although, in principle, our Cycle 0 ^{12}CO $J = 2$–1 data can help constrain the above more stringently, since the beam for the latter is much larger, the waist emission cannot be adequately isolated from the bipolar outflow emission.

3.2. CO(J = 1–0) Imaging

The ^{12}CO $J = 1$–0 mapping (12 m mosaic + ACA), together with total-power (TP) data recovers all of the flux lost in the Cycle 0 data and reveals previously unseen distant regions. Due to some ISM emission present in the reference OFF position in the TP data, there is an absorption spike at −16.7 km s^{-1}.

A moment 0 map of the CO $J = 1$–0 absorption+emission, integrated over the velocity range of $-171 < V_{\rm lsr}$ (km s^{-1}) $<$ 144, from this data set (beam 4.″1 × 1.″8), reveals a mild large-scale asymmetry in the envelope—the ultra-cold region (seen in magenta/dark blue) is slightly more extended N-S (Figure 7). In spectra extracted from annuli with increasing average radii, the absorption signal can be detected out to the outermost edge of our map (Figure 8). The line profile tends to get narrower as the average annulus radius increases.

The true envelope size in CO is difficult to determine. We can only determine a lower limit from the data because of the rather pathological conditions in this object, specifically that the CO from the ultra-cold envelope is in absorption. This signal weakens at larger radii, which can result from a warming of the outermost layers and/or a decrease in optical depth such

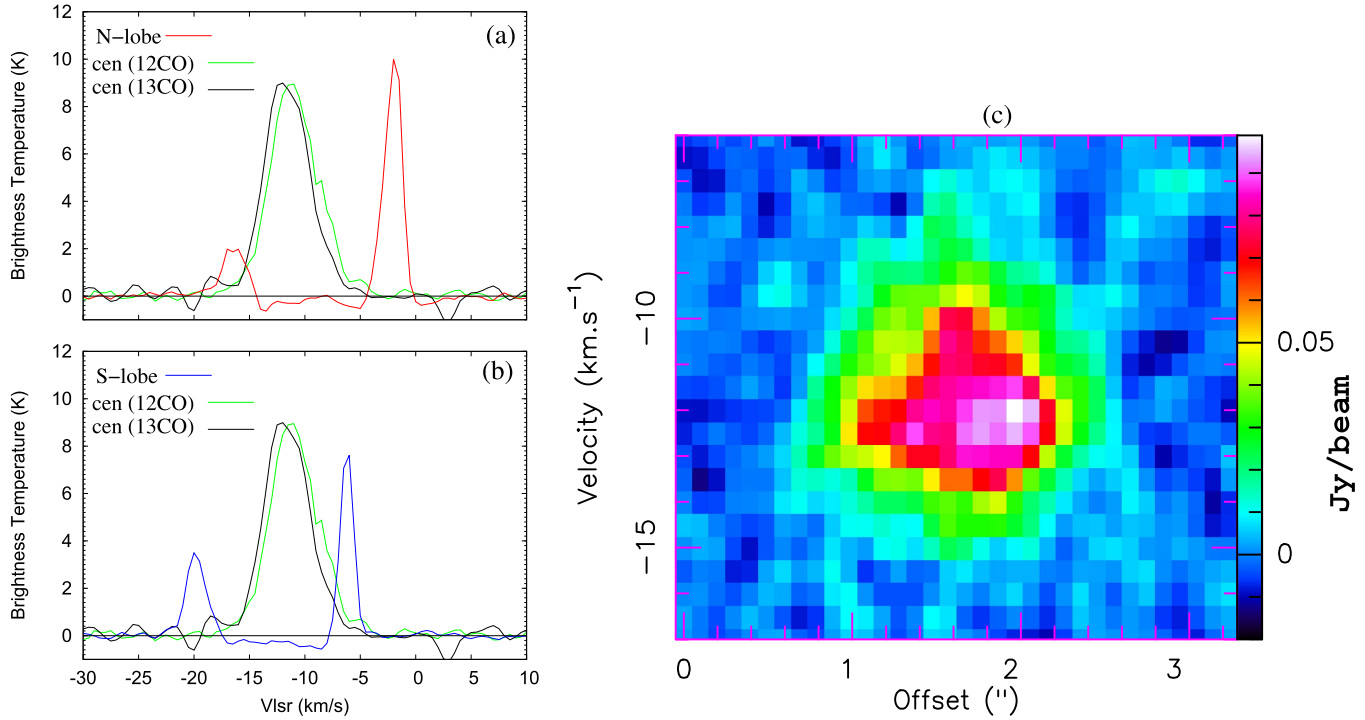

Figure 6. (a, b) ^{12}CO $J = 3$–2 spectra extracted from the northern (red) and southern (blue) lobes of the Boomerang. The ^{12}CO and ^{13}CO 3–2 spectra from the central waist in green (scaled by 0.5) and black (scaled by 0.95) are shown in each panel for comparison. (c) Position–velocity cut of the ^{13}CO $J = 3$–2 intensity, taken along the major axis of the waist of the Boomerang.

that it becomes optically thin in the CO $J = 1$–0 line, causing line excitation temperature to equilibrate with the microwave background temperature. Even the decrease in velocity width that we observe at large radii is not necessarily an indicator that we are getting close to the edge of the CO envelope, because the above effects will also restrict the total velocity spread of material observed in absorption along the line of sight.

Using the TP map, that has the largest FOV, we extract spectra from a few annuli, with the outermost one having an outer radius close to the edge of the FOV (Figure 9). A significant absorption signal can be detected in the 76.″5–86.″5 annulus, i.e., at an average radius of about 80″. The line profile tends to get narrower as the average annulus radius increases.

3.2.1. Physical Properties of the Ultra-cold Outflow

Our new ALMA CO $J = 1$–0 map of the Boomerang, combining the 12 m mosaic with ACA mapping and TP data, shows the presence of the ultra-cold outflow out to a radius of at least 80″, significantly larger than that inferred by SN97. This finding, together with the discovery of the radially increasing expansion velocity that we reported in Setal13, warrants a re-examination of the mass-loss rate and total mass in the ultra-cold outflow.

In the ultra-cold outflow, since the excitation temperature of the $J = 1$–0 line, $T_{\rm exc}(1\text{–}0)$, is below the microwave background, $T_{bb} = 2.725$ K, virtually all of the CO population is in the $J = 0$ level, and the tangential optical depth in the $J = 1$–0 line, $\tau_{1,0}$, at any impact parameter p, is relatively insensitive to the exact value of $T_{\rm exc}(1\text{–}0)$. We can therefore analytically express $\tau_{1,0}$ as a function of a radially variable mass-loss rate, $\dot{M}_0\,[V\,(r)/V_0]^a$, and a linearly increasing outflow velocity, $V_r = V_0\,(r/R_0)$ (see Equation (12) in the Appendix). We set $V_0 = 164$ km s^{-1} and $R_0 = 80''$. Since $\tau_{1,0} \gtrsim 1$ if $T_{\rm exc}(1\text{–}0) < T_{bb}$, then setting $\tau_{1,0} \gtrsim 1$ at an angular radius, $r = 80''$, and assuming a constant mass-loss rate (i.e., $a = 0$), $dM/dt = \dot{M}_0$, we find that $\dot{M}_0 \gtrsim 2.1 \times 10^{-3}$ $M_\odot$ yr^{-1}. Making conservative assumptions about the value of the outflow inner radius, $r_{\rm in} = 6''$, and the fractional CO abundance for a C-rich star (determined by the O abundance, assuming complete association of O into CO), $f_{\rm CO} = 1.3 \times 10^{-3}$, the total mass in the ultra-cold outflow is $M_{\rm cold} \sim 19 M_\odot \ln(6''/r_{\rm in})\,(1.3 \times 10^{-3}/f_{\rm CO})$ (Equation (13) in the Appendix). For an O-rich object, $f_{\rm CO}$ is lower (0.66×10^{-4}: determined by the C abundance, assuming the complete association of C into CO), requiring an even larger mass (by a factor of two) for the slow outflow.[5] Thus, assuming that the Boomerang has evolved from an RGB[6] or AGB star (which implies that its main-sequence mass is $M_{\rm ms} \lesssim 8\ M_\odot$), the inferred values of $M_{\rm cold}$ are unacceptably large.

We therefore conclude that the mass-loss rate in the ultra-cold outflow is not uniform. The value of $M_{\rm cold}$ can be reduced if we assume that the mass-loss rate in the ultra-cold outflow increases with the outflow velocity, i.e., $a > 0$, provided $\tau_{1,0} > 1$ in its inner regions, $r \gtrsim r_{\rm in}$. Using Equation (14) (see the Appendix), we find that $a \gtrsim 0.9$, since the maximum mass that can be ejected in the ultra-fast outflow is $M_{\rm cold} \lesssim 7.3\ M_\odot$, assuming that the mass of the Boomerang's central (post-AGB) is comparable to the typical masses for the central stars of planetary nebulae (which lie in a relatively narrow range, peaking at $\sim$0.61 $M_\odot$: Gesicki & Zijlstra 2007), and accounting for the (relatively small) mass ejected in the inner outflow ($\sim$0.13 $M_\odot$: SN97).

We can set an upper limit on a from the requirement that both the ^{12}CO and ^{13}CO $J = 1$–0 lines must remain optically thick in

[5] Although it is more likely that the Boomerang is O-rich (see Section 3.3), the constraints that we derive in this section are intentionally conservative, employing the lower value of $\dot{M}_0$ based on assuming it to be C-rich.

[6] RGB = Red Giant Branch.

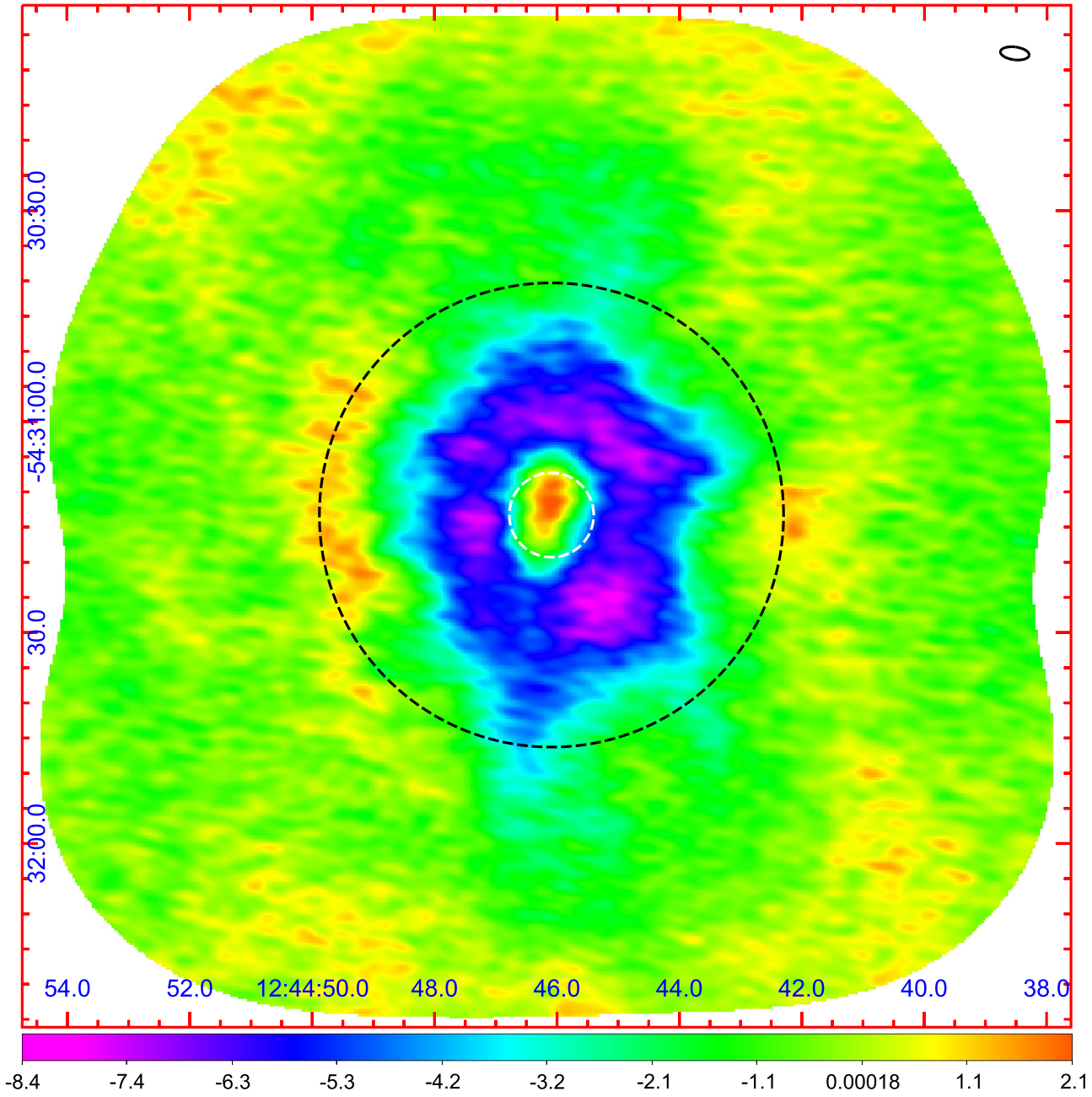

Figure 7. CO $J = 1$–0 moment 0 map of the Boomerang, covering the velocity range, $-171 < V_{\rm lsr}\,({\rm km\ s^{-1}}) < 144$. The black (white) dashed circle denotes the size of the SN97 model ultra-cold outflow (inner outflow). The color scale is in units of Jy−km/s beam^{-1}; the beam size (FWHM) is shown at the top right corner. The 1σ noise is 0.4 Jy-km/s beam^{-1}.

the inner regions of the ultra-cold outflow in order to keep their excitation temperature there below T_{bb}. Specifically, as per the SN97 model, $\tau_{1,0} = 5.2$ at $r = 10''$,[7] which implies, using $\tau_{1,0} \propto r^{a-3}$ (Equation (12) in the Appendix), that $a \lesssim 2.2$, $M_{\rm cold} \gtrsim 3.3\ M_\odot$, and $M_{\rm ms} \gtrsim 4\ M_\odot$. In order to maintain $\tau_{1,0} \geqslant 1$ at $r = 80''$ (see above), Equation (12) (see the Appendix) implies that $\dot{M}_0$ must increase as $D^{3-a} = D^{(0.8-2.1)}$. Hence, in order to keep $M_{\rm ms} \lesssim 8\ M_\odot$, the distance must be $\lesssim$4 kpc.

The Boomerang has an anomalously low luminosity, even at its maximum allowed distance of 4 kpc, of $<$2130 $L_\odot$. For example, for a post-AGB object that has evolved from a star with $M_{\rm ms} \gtrsim 4\ M_\odot$, post-AGB evolutionary tracks show that the luminosity in the early post-AGB phase is $\gtrsim 2 \times 10^4\ L_\odot$ (e.g., Vassiliadis & Wood's 1994, Miller Bertolami 2016).

It is possible that the Boomerang is a post-RGB or post-EAGB[8] object, similar to the class of low-luminosity ($L \sim$ 100–2500 $L_\odot$), dusty evolved objects recently discovered in the Magellanic Clouds (Kamath et al. 2016). The Boomerang is not the only evolved star with an anomalously low luminosity; as noted by SN97, the very young PN, M 1-16, which is similar to the Boomerang in being a young bipolar PN and having a very low ^{12}CO/^{13}CO abundance ratio, shares the same low-luminosity issue as the Boomerang (Sahai et al. 1994).

[7] Note that $\tau_{1,0} > 3.3$, since the ^{13}CO $J = 1$–0 line also shows absorption, and the ^{12}CO/^{13}CO abundance ratio is $\geqslant$3.3 (SN97).

[8] EAGB = Early Asymptotic Giant Branch.

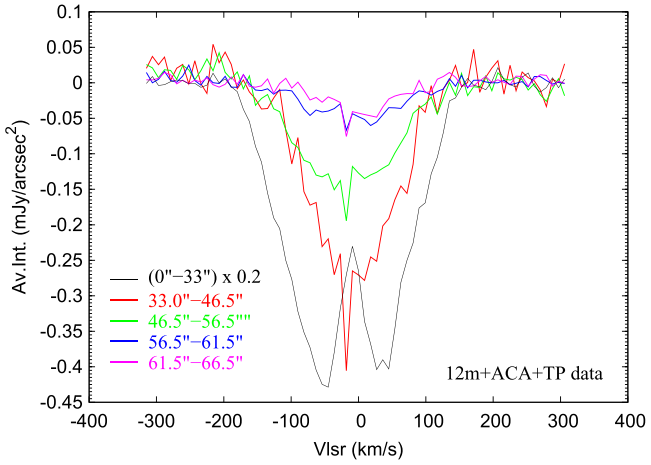

Figure 8. CO $J = 1$–0 spectra extracted from the combined datacube, using annular apertures of increasing average radius.

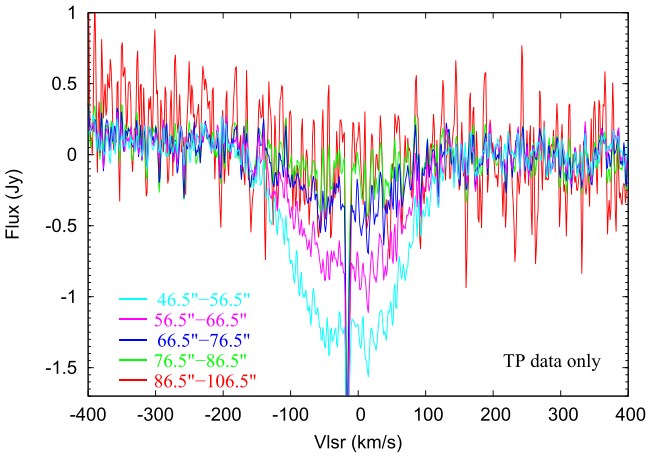

Figure 9. CO $J = 1$–0 spectra extracted from the TP datacube, using annular apertures of increasing average radius.

3.3. Discovery of SO Emission

We find the unexpected presence of the weak SO line (N, $J = 2, 3$–$1, 2$ at 99.299 GHz) emission (Figure 10) toward the central region of the Boomerang. Although the SO map is relatively noisy, the line emission is not centered on the 3 mm continuum source but appears to be associated with the base of each the N and S lobes. The intrinsic line-width is 79 km s^{-1} (inset, Figure 10), after deconvolving the limited spectral resolution of the continuum spectral window in which the line was found (15.625 MHz).

In the past, the general lack of molecular emission lines from oxygen-bearing molecular species (except CO) in the Boomerang Nebula, had suggested to us that the latter is C-rich. For example, although OH masers are often seen in O-rich PPNe (e.g., Sahai et al. 2007), no OH maser emission has ever been found in the Boomerang. Our detection of SO in the Boomerang now suggests that the nebula is possibly O-rich, since SO is not expected to be present in the outflows of C-rich AGB stars, and has not been found so far in C-rich objects. Additional support for this inference comes from the detection of an H_2O line in the Boomerang (Bujarrabal et al. 2012). Furthermore, if, as proposed above (Section 3.2.1) and argued later (Section 4), the Boomerang is a post-RGB or post-EAGB object, then it would not be expected to be C-rich.

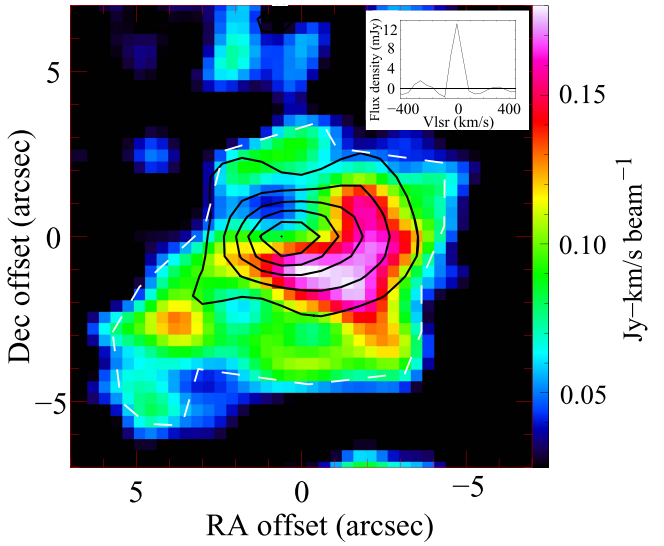

Figure 10. Moment 0 map of the SO N, $J = 2, 3$–$1, 2$ line emission (color scale), overlaid with the 92 GHz continuum emission (contours) toward the Boomerang. The minimum contour (step) is 25% (15%) of the peak intensity, 3.37×10^{-4} Jy km s^{-1} beam^{-1}. The beam for the SO (continuum) data is $2\farcs38 \times 1\farcs81$, PA $= -87\fdg4$ ($2\farcs60 \times 1\farcs97$, PA $= -89\fdg1$). Inset shows the SO line profile, extracted from a polygonal aperture (dashed line).

However, the SO and H_2O detections are not totally conclusive about the Boomerang's O-rich nature, since H_2O has been found in C-rich post-AGB objects (e.g., CRL 618, CRL 2688, and NGC 7027: Bujarrabal et al. 2012). SO may be produced in the Boomerang as a result of shock-driven chemistry in the interaction between the inner bipolar outflow and the outer ultra-cold outflow, possibly involving dust sputtering that releases S locked up as solid MgS in grains (e.g., *ISO* observations show a strong 30 μm feature in C-rich evolved stars attributed to MgS: Hony et al. 2002).

In light of our discovery of SO, we have searched for the presence of additional weak lines. We imaged the entire band 3 SPWs. For the band 3 "high" SPWs, that cover the 99.75–103.5 GHz and 111.75–115.5 GHz frequency ranges, we made images at 10 channel (4.8826 MHz) resolution for our 12m-mosaic data (we did not include the ACA because it does not add much additional sensitivity). We found no indication of any lines, apart from CO $J = 1$–0. For the band 3 "low" SPW's, that cover the 83.01–88.01 GHz and 96.01–98.01 GHz frequency ranges, we made images with single channel spectral resolution (15.6 MHz). We found no indication of any other lines, apart from the SO line mentioned above. The frequency region covered in these data, excluding bad channels, does not cover any additional SO line.

3.4. Continuum Imaging and Dust Mass in the Dense Waist

We observed the continuum emission at 3.3 mm and 0.88 mm toward the Boomerang. At 0.88 mm, the waist shows an unresolved core with a faint extension along the EW direction; the beam is $0\farcs43 \times 0\farcs35$ at PA $= 42.4$ (Figure 11). The peak intensity is 2.7 ± 0.1 mJy/beam, and the noise in the image is about 0.06 mJy/beam. At 3.3 mm (beam $2\farcs60 \times 1\farcs97$ at PA $= -89\fdg1$), there is a bright central source that is extended along the EW direction, with a half-power size

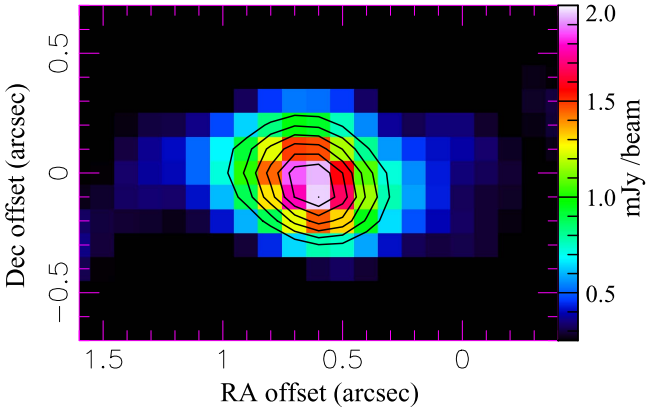

Figure 11. 0.87 mm continuum emission from the Boomerang. The continuum peak is located at (J2000) R.A. = 12:44:46.081, decl. = −54:31:13.38, whereas the phase center (i.e., offset 0,0) is located at (J2000) R.A. = 12:44:46.01, decl. = −54:31:13.32. Minimum contour level (step) is 40% (10%) of the peak, 1.96 mJy/beam. Beam (FWHM) is $0\farcs43 \times 0\farcs35$, at PA = 42°.4.

that is $3\farcs9 \times 2\farcs5$ (Figure 10, contour map). In addition, there is faint, structured, extended emission N and S of the central source, with peak intensities in the range of 0.07–0.09 mJy/beam. The noise in the 3.3 mm image is in the range of 0.015–0.02 mJy/beam.

We revise the Setal13 model of the radio-to-(sub)millimeter-wave SED (Table 2), using both cycle 0 and cycle 1 continuum measurements (Figure 12), extending the wavelength coverage of the millimeter-submillimeter SED over a much larger wavelength span, thus enabling a more robust estimation of dust properties. The fluxes were extracted from images convolved to the same beam as used in the lower-resolution Cycle 0 data ($4\farcs1 \times 2\farcs9$ at PA = −33°.9), using an aperture of size $6'' \times 4''$ that encompasses most of the emission. The dust emission is optically thin at all wavelengths: e.g., even with the dust temperature, T_d, as low as 5–10 K, the peak optical depth at 0.88 mm, estimated from its peak intensity, is about 0.09–0.015. Assuming a power-law dust emissivity $\kappa(\nu) \propto \nu^{\beta}$, and using the fluxes at the maximum and minimum frequencies of our observed range (i.e., 338.4 and 92.0 GHz), we find that $\beta \sim 0$ in the Rayleigh–Jeans (R–J) limit. However, β may be higher if T_d is low enough to make the R–J approximation inaccurate (Setal13). For example, if T_d = 15, 20, 25, 30, 35 K, then β = 0.3, 0.21, 0.16, 0.12, 0.1.

We follow Setal13's reasoning to constrain T_d, using the deconvolved half-power size of the continuum source measured at 3.3 mm, $\sim 2\farcs3$ (giving a characteristic radius of $\sim 2.6 \times 10^{16}$ cm for the dust source). The dust radius at a given value T_d is, $r_d = (L_* T_*^{\beta}/16\,\pi\,\sigma)^{1/2}\, T_d^{-(2+\beta/2)}$ (e.g., Herman et al. 1986), for heating by a central stellar source with luminosity and temperature of L_* and T_* (where σ is the Stefan-Boltzmann constant). If the dust grains in the Boomerang's waist are heated directly by starlight, then T_d, β = (32 K, 0.11). If, as is more likely, there is substantial extinction and reddening due to the inner parts of a central disk, and we conservatively assume that only 10% of the total stellar flux, reddened to 900 K is available for heating, then T_d, β = (19 K, 0.22). We conclude that the continuum emission source in the central region of the Boomerang has $T_d \sim$ 19–32 K, β = 0.1–0.2 with a dust mass (4–7) $\times 10^{-4}$ $M_{\odot}$. Comparable or larger masses of such grains have also been found in the central regions of other PPNe and disk-prominent post-AGB objects (e.g., Sahai et al. 2011).

The very low value of β and the lack of observable steepening of the spectral index of the SED toward the largest wavelength observed with ALMA, 3.5 mm, suggests that the grains may have sizes in the cm range. For example, in an extensive laboratory study of grains by Pollack et al. (1994), the lowest values of β are 0.23–0.87 for composite[9] grains of 3 cm radius at temperatures of 700–100 K. Compared to composite grains, segregated[10] grains give lower values of β for the same grain-size and temperature, e.g., β = 0.31–1.08 for 3 mm radius grains at temperatures 700–100 K, compared to β = 0.86–1.34 for composite grains. Taking into account the inverse relationship between β and temperature for the laboratory grains, and the relatively low temperature derived for the dust grains in the Boomerang, even if the grains in the Boomerang are segregated, it appears likely that the grain sizes are >0.3 cm.

We now discuss and discard two alternative mechanisms for explaining the shallow millimeter–submillimeter spectral index found above—spinning dust grains and ferromagnetic or ferrimagnetic nanoparticles. Spinning dust grains produce centimeter-wave emission, generally peaking around ∼40 GHz (e.g., Draine & Lazarian 1998); however, under special circumstances the emission peak can shift to higher frequencies (Silsbee et al. 2011), and thus could contribute at millimeter wavelengths. Silsbee et al. (2011) show plots of the SED due to spinning dust for 6 different astrophysical environments—among these, reflection nebulae (RN) and photodissociation regions (PDR) peak at millimeter wavelengths. However, in the RN model, the emission peak is at ∼85 GHz and falls relatively sharply for higher frequencies (e.g., Equation (9) of Draine & Hensley 2012: DH12), so it does not provide enough flux in the 1.3–0.87 mm range to explain the Boomerang's observed shallow spectral index in this range. The PDR model peaks at a higher frequency (∼170 GHz) but it is characterized by an ionizing radiation field that is a factor of 3000 times the intensity of the ambient Galactic starlight, inconsistent with the relatively low radiation-intensity environment present in the Boomerang waist region. We conclude that spinning dust grains cannot explain the shallow spectral index of the millimeter–submillimeter SED in the Boomerang.

Emission from ferromagnetic or ferrimagnetic nanoparticles in the centimeter–submillimeter wavelength range, where these materials have enhanced absorptivity, has been proposed by Draine & Hensley (2013) to explain the observed strong millimeter-wave emission from a number of low-metallicity galaxies, including the Small Magellanic Cloud (DH12). From Figure 12 of Draine & Hensley (2013), the spectral index for the millimeter–submillimeter SED resulting from various types of Fe-bearing nanoplarticles is roughly consistent with that of the Boomerang's millimeter–submillimeter SED.

We scale the predictions for the emission from different kinds of Fe nanoparticles (radius $a = 0.01\ \mu$m) in models of the SMC SED by DH12, to obtain an estimate of the dust mass in Fe-nanoparticles, $M_{d,Fe}$, required to produce the observed (say) 100 GHz flux in the Boomerang (∼0.6 mJy). From Figures 3–4 of DH12, we find that F_{ν} (100 GHz) ∼ 0.09 mJy $(D/62\ \mathrm{kpc})^2$ $(M_{d,\mathrm{Fe}}/1\ M_{\odot})$, implying that for the Boomerang, $M_{d,\mathrm{Fe}} = 3.9 \times 10^{-3}\ M_{\odot}$. Assuming a cosmic abundance of Fe

[9] Individual grains contain multiple dust species, with 50% of void volume.
[10] Individual grains contain only one dust species.

Table 2
Boomerang Nebula Continuum Emission

ν GHz	Peak Intensity[a] mJy beam^{-1}	rms mJy beam^{-1}	Flux Density[b] mJy	Comment
85.01	0.409	0.039	0.429	Individual SPW
87.01	0.425	0.036	0.417	Individual SPW
97.08	0.521	0.047	0.536	Individual SPW
99.01	0.615	0.050	0.599	Individual SPW
92.02	0.452	0.022	0.456	All SPW
107.47	0.640	0.041	0.686	Cycle 0
107.52	0.808	0.077	0.821	All SPW
236.40	3.650	0.334	3.351	Cycle 0
331.39	6.857	0.946	5.331	Individual SPW
333.13	5.911	0.732	5.232	Individual SPW
343.32	6.113	0.798	5.313	Individual SPW
345.23	5.925	0.878	4.970	Individual SPW
338.39	6.705	1.001	5.877	All SPW

Notes.
[a] All images have been convolved to a common beam-size $4\farcs1 \times 2\farcs9$.
[b] Flux density determined using a common aperture of size $6'' \times 4''$ for all wavelengths.

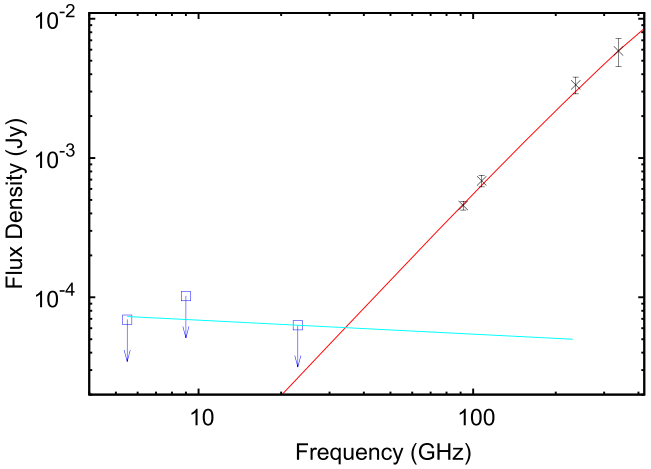

Figure 12. Radio to millimeter-wave SED of the Boomerang. Error bars for the ALMA data (black crosses) are $\pm 1.5\sigma$. The ATCA data show (blue squares) $\pm 3\sigma$ upper limits. The ALMA data have been fitted with optically thin dust emission from large grains with temperature 30 K and a power-law emissivity index, $\beta = 0.11$ (red curve). The ATCA upper limits have been fitted with optically thin free–free emission (cyan curve).

(Fe/H $= 4 \times 10^{-5}$) and that 100% of all the available Fe is in these small grains, the associated gas mass of $1.8\,M_{\odot}$ is implausibly large for the waist region of the Boomerang.

3.5. Optical Polarization

The optical polarization pattern (Figure 13(a)) is generally centro-symmetric around the location of the central star (i.e., polarization vectors have an azimuthal orientation) in most regions of the nebula except in the waist region, and the polarized light fraction is quite high, with values as high as ∼60% in the bright walls of the lobes—typical of a singly scattering reflection nebula (e.g., Sahai et al. 1999) with small grains of size ∼0.1 μm (see Table 1 of Jura 1975). In the dense waist, the percentage polarized is significantly lower, most likely due to multiple scattering in an optically thick medium.

In the central region, a remarkable S-shaped structure can be seen in the polarized intensity image (Figure 13(b)). The polarization vectors in this structure show a striking departure from the centro-symmetric pattern. For example, in the northern and southern spurs of this structure, the vectors are oriented along the position angle of the spurs, and the polarized fraction is quite high in these regions, about 50%. Such a high level of polarization can only be explained by single-scattering off dust grains. The orientation of the polarization vectors at an intermediate angle between the azimuthal direction and the radial direction suggests the presence of a radial polarization component, in addition to the expected azimuthal one.

Radial polarization has been observed by Woodward et al. (2011) in the optical and near-IR, at scattering angles of ∼0°–20°, from their observations of comet C/2007 N3 (Lulin)—these authors state that such "optical negative branch polarization" behavior is observed in most comets at small ($\lesssim$25°) phase angles. Canovas et al. (2015) show, using the Mie theory (Mie 1908) that different types of grains can rotate the plane of polarization from perpendicular (producing an azimuthal polarization pattern) to parallel (producing a radial polarization pattern). They find negative polarizability (leading to radial polarization) for grains of different properties when the scattering angle lies in the ranges ∼15°–60° and 140°–160° (see Figure 1(b) of Canovas et al. 2015).

Based on the results of these studies, we hypothesize that the polarization pattern observed in the spur structures in the Boomerang is a result of optical negative branch polarization due to a fortuitous location of the spurs within the lobes, such that some fraction of the material within them provides scattering angles for which the polarizability is negative. For example, if some sizable fraction of the southern and northern spurs lie along a common axis with inclination, $\theta_{\rm spur}$ relative to the line of sight (los), then for (say) $\theta_{\rm spur} = 20°$–40°, the scattering angles of these regions in the southern (northern) spur are 20°–40° (160°–140°), i.e., within the negative polarizability angle ranges in the Canovas et al. (2015) models. Material in the spurs that subtend scattering angles outside these ranges would have positive polarizability, and the combination of radial and azimuthal polarization vectors could then produce the observed intermediate orientation. Note that for our hypothesis to work, it is essential that the spur material

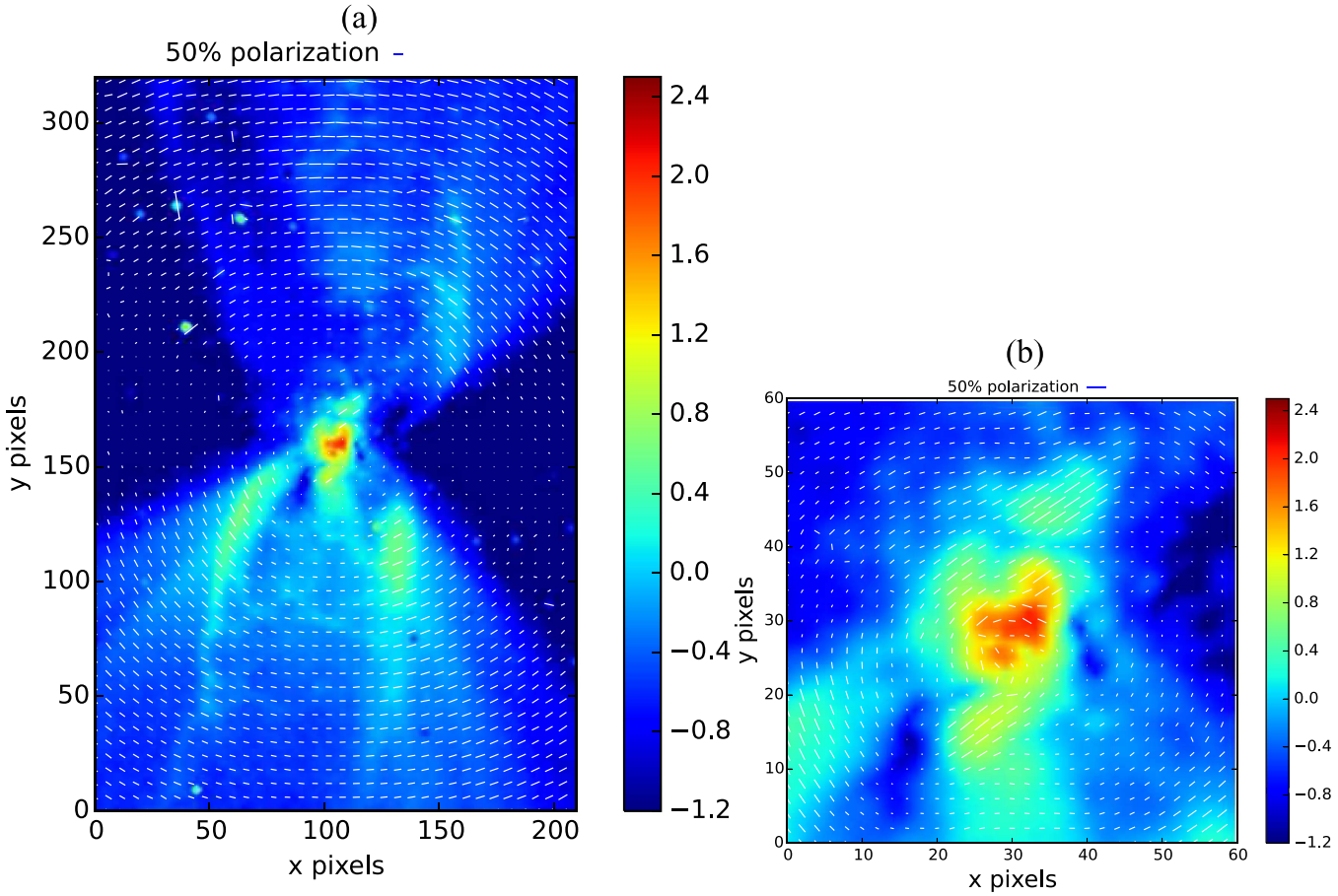

Figure 13. Optical polarization in the Boomerang Nebula as observed with *HST*/ACS. (a) The 0.6 μm polarized light intensity image (log stretch) overlaid with vectors showing the polarization angle and percentage polarization. (b) Same as in *a*, but for the central region. Color bars show the log of the intensity, i.e., log10 (DN pixel^{-1}), where 1 DN = 5.016 × 10^{-19} erg s^{-1} cm^{-2} Å^{-1}. The angular scale is 0.″025 pixel^{-1}.

lies within a compact region along the los, implying that the S-shaped structure is filamentary. We speculate that this structure may be due to a precessing jet.

4. Ejection Timescales and Binary Interaction Models

We estimate a lower limit on the expansion age of the ultra-cold outflow of 3480 years (from R_0/V_0). Comparing this with the ages of the bipolar lobes, and the central waist, we find that the ultra-cold outflow is the oldest, followed by the waist[11] (∼1925 years), and the youngest is the fast bipolar outflow(s) (⩽1050 years) that interacts with the ultra-cold outflow to produce the N- and S-lobes. Thus the temporal sequence of waist-formation followed by the ejection of a collimated fast outflow, in the Boomerang, is similar to that derived by Huggins (2007) for a small sample of similar objects (late AGB stars, PPNe and young PNe). Huggins shows that this sequence naturally favors the class of models in which a companion interacts directly with the central star. These include two subclasses of models: (A) the build-up of a torus enhances the accretion rate in a disk around a companion that then drives jet-like outflows, or (B) both spin-up and ejection of the stellar envelope of the primary occur during a common-envelope (CE) phase as the companion spirals into the center of the AGB star.

We note that the time periods between the CSE ejection, torus ejection, and high-velocity outflow formation in the Boomerang (1555 years and ⩾875 years) are much larger than the corresponding durations for the "water-fountain" PPN, IRAS 16342-3814, in which these are about 300 years and 50 years (Sahai et al. 2017). An inspection of the nine objects in Huggin's study (see his Table 1) reveal that only one has a similarly long "jet-lag" (i.e., torus age minus the fast outflow age; KjPn 8: 1660 years), as the Boomerang. Six of the remaining eight have significantly shorter jet-lags (∼270–390 years), and two have intermediate jet-lags (∼510–690 years). Quantitative models that can provide estimates of the "jet-lag" have the potential of discriminating between subclass A and B models, and constraining the relevant physics.

In the case of the Boomerang, we show that model B is needed in order to explain the extreme properties of the ultra-cold outflow. The very high mass-loss rate, radially increasing and high expansion velocity of the ultra-cold outflow, coupled with the low luminosity of the Boomerang, imply that the standard model for a dusty, molecular outflow from an evolved star, i.e., one driven by radiation pressure on dust, is not applicable. The ultra-cold outflow's mass-loss rate of $>10^{-3}$ $M_\odot$ yr^{-1} is orders of magnitude above typical values for the RGB or EAGB ($\lesssim 10^{-6}$ $M_\odot$ yr^{-1} for $L \lesssim 2500$ $L_\odot$, Groenewegen 2012). The kinetic energy of the ultra-cold outflow is very high, $KE_{\rm cold} > 4.8 \times 10^{47}$ erg (using Equation (15) in the Appendix).

We propose that the most likely source of this energy is the gravitational energy released via binary interaction in a

[11] Assuming its outer region is expanding.

common-envelope event (CEE). The latter is given by the difference in orbital energies of the binary before and after the interaction, i.e.,

$$E_{\rm CEE} = \frac{G\,M_2\,M_{1,c}}{2\,a_f} - \frac{G\,M_2\,M_1}{2\,a_i}, \quad (1)$$

which can be rewritten as

$$E_{\rm CEE} = \frac{G\,M_2\,M_{1,c}}{2\,a_f}\,\eta(M_1, M_{1,c}, a_f, a_i), \quad (2)$$

where $\eta(M_1, M_{1,c}, a_f, a_i) = 1 - (M_1/M_{1,c})(a_f/a_i)$, M_1 ($M_{1,c}$) is the initial (final) mass of the primary, M_2 is the companion mass, and a_i (a_f) is the initial (final) semimajor axis of the binary.

The released energy must be equal to, or exceed, the kinetic energy in the ultra-cold outflow plus the energy required to unbind the envelope, $|E_{\rm bind}| - \Delta E_{\rm therm} - \Delta E_{\rm other}$, where $E_{\rm bind}$ is the binding energy of the envelope, $\Delta E_{\rm therm}$ is the thermal energy of the envelope, and $\Delta E_{\rm other}$ can include contributions from recombination, nuclear fusion,[12] and accretion[13] (Ivanova et al. 2013). Since estimating the value of $|E_{\rm bind}| - \Delta E_{\rm therm} - \Delta E_{\rm other}$ depends on several uncertain parameters (Ivanova et al. 2013), we first set it equal to zero. Hence,

$$E_{\rm CEE} > KE_{\rm cold}, \quad (3)$$

from which we can derive an upper limit on the separation of the final binary.

Taking $M_1 = 4\ M_\odot$, and typical values for $M_{1,c} = 0.6\ M_\odot$, $M_2 = 1\ M_\odot$, and setting $\eta \sim 1$ (since $a_i \gg a_f$), we find that $2\,a_f < 4.7\ R_\odot$. However, because the radius of the Boomerang's central star, estimated to be $\sim 16\,R_\odot$, from its effective temperature, $T_{\rm eff} = 6000$ K and $L \sim 300\ L_\odot$, is significantly larger than $2\,a_f$, it is likely that the companion merged with the primary after the in-spiral.

The Boomerang Nebula thus appears to have resulted from a strongly interacting binary system, in which a very significant fraction of the primary star's envelope was ejected while it was on the RGB or EAGB, as the companion spiraled in toward the latter's core. This ejection contains material covering a large range of velocities (up to a maximum of about 164 km s^{-1}), and produces the ultra-cold outflow. At the end of the in-spiraling event, the companion merges with the primary. During the in-spiral, a large disk is created around the central star. The disk powers a fast collimated outflow that interacts with the ultra-cold outflow to produce the central bipolar nebula. In this scenario, the age of the waist must be less than that of the ultra-cold outflow, i.e., $\lesssim$3480 years.

A potential difficulty with the ultra-cold outflow resulting from CEE is that the former's morphology does not appear to be concentrated toward the equatorial plane, as has been found in numerical simulations of CEE (e.g., Iaconi et al. 2017, and references therein). However, a detailed inspection of the simulation in Iaconi et al. (2017), shows that the mass distribution of the ejecta appears to become more isotropic with time (see their Figure 5, right-hand panel). In Figure 8 of Iaconi et al. (2017), which shows the masses ejected in three pairs of pyramids oriented at the center of the computational cube and whose bases are the six faces of this cube, the masses in the x- and y-pyramids (these encompass the equatorial plane) appear to approach that in the z-pyramid (which encompasses the polar direction) at 2000 days after the onset of the interaction, with only a factor of three difference between the mean mass in the x- and y-pyramids, compared to the z-pyramid.

Given that we are observing the Boomerang ultra-cold outflow at an age that is a factor of $\sim$650 larger than the 2000 day timespan of Iaconi et al.'s simulation, it is not implausible that the lower-density polar regions seen on small scales in the simulation get filled in with time (e.g., small perturbations in the velocity vectors away from radial would allow material to move toward the axis). Furthermore, the Iaconi et al. (2017) simulation assumes a much less massive primary (0.88 $M_\odot$ RGB primary) than the Boomerang's; it is possible that for a more massive RGB star, the CEE ejection is more isotropic.

New CEE simulations, with more massive primary stars, that can reproduce the relatively well-defined properties of the Boomerang Nebula, will be very useful in improving our understanding of an important channel for binary star evolution.

5. Conclusions

We have obtained ALMA maps of millmeter-wave line and continuum emission at the highest-angular resolution to-date of the Boomerang Nebula, the coldest known object in the universe.

1. The high-resolution ^{12}CO $J = 3$–2 imaging of the inner outflow of the Boomerang reveals a detailed correspondence between the molecular gas and the dust as seen in scattered light via optical *HST* imaging. Both the molecular-line and the optical images shows that the N-lobe has a complex multipolar structure, whereas the S-lobe has a relatively simple (largely cylindrical) geometry.
2. A dense central waist of size (FWHM) $\sim$1740 au $\times$ 275 au, separates the N- and S-lobes, and is expanding much more slowly than the lobes. The velocity width of the ^{12}CO and ^{13}CO $J = 3$–2 line profiles is the smallest seen toward a sample of PPNe, and is similar to that seen in the rotating disks of post-AGB objects like the Red Rectangle. A position–velocity cut of the ^{13}CO $J = 3$–2 taken along the major axis of the waist shows more complex kinematics than simple expansion, possibly due to the presence of a Keplerian rotational component.
3. The ultra-cold outflow in the Boomerang Nebula extends to a radius of at least 80″ (120,000 au). The mass-loss rate in the ultra-cold outflow ($\geqslant 2.1 \times 10^{-3}\ M_\odot\ {\rm yr}^{-1}$ at $r = 80''$) is not uniform, but increases with radius, similar to its expansion velocity, which also increases with radius (Setal13). The mass in the ultra-cold outflow is $\gtrsim$3.3 $M_\odot$, and the mass of the Boomerang's main-sequence progenitor is $\gtrsim$4 $M_\odot$.
4. The expansion age of the ultra-cold outflow is $>$3480 years. The central waist (assuming its outer region is expanding) and fast bipolar outflow are younger, with expansion ages of $\sim$1925 years and $\leqslant$1050 years. The "jet-lag" (i.e., torus age minus the fast-outflow age) in the Boomerang lies within (and near the upper end of) the range of values found for other AGB or post-AGB

[12] Due to a non-compact companion, e.g., a main-sequence star, filling its Roche lobe and causing H-rich materal to fall onto primary's core.
[13] Onto the companion during its in-spiral.

objects with jets and torii, and suppports models in which the primary star interacts directly with a binary companion.
5. The relatively shallow slope of the submillimeter–millimeter SED for $\lambda = 1.3$–2.6 mm found in our previous study, applies over a much broader wavelength window, $\lambda = 0.87$–3.5 mm. We infer that the grains are cold (19–32 K), and that the dust absorption power-law exponent ($\kappa \propto \nu^{\beta}$) is, $\beta = 0.1$–0.2, implying the presence of very large (few millimeter to centimeter sized) grains. Alternative models for producing the low value of β such as spinning grains or Fe-containing nanoparticles are very unlikely.
6. The nebula is highly polarized at optical wavelengths, and the polarization pattern is generally centro-symmetric around the location of the central star in most regions of the nebula, typical of a singly scattering reflection nebula with small grains ($\sim$0.1 μm). In the dense waist, the percentage polarized is significantly lower, most likely due to multiple scattering in an optically thick medium.
7. In the central region, an S-shaped structure is seen in the polarized intensity image, and the polarization vectors in this structure show a striking departure from the centro-symmetric pattern. We hypothesize that this pattern results from the contribution of a radial polarization component due to scattering by dust grains at angles for which the polarizability is negative.
8. We find the presence of SO in the central region of the Boomerang. This result, taken together with a previous detection of H_2O, suggests that the Boomerang Nebula is O-rich.
9. The Boomerang Nebula was most likely produced by a common-envelope binary interaction, while the primary was an RGB or early-AGB star, with the companion spiraling into and finally merging with the primary's core, and ejecting the primary's envelope that now forms the ultra-cold outflow.

We thank an anonymous referee for remarks that have helped improve our paper. We thank Orsola De Marco for reviewing and providing comments on our discussion of the inspiral energetics, and Eric Blackman for his thoughts on the possibility of isotropic ejection during CEE. We thank Misty Cracraft (STScI) for providing us with the calibrated *HST* polarization data on the Boomerang in digital form. This paper makes use of the following ALMA data: ADS/JAO. ALMA#2012.0.00510.S. ALMA is a partnership of ESO (representing its member states), NSF (USA), and NINS (Japan), together with NRC (Canada) and NSC and ASIAA (Taiwan), in cooperation with the Republic of Chile. The Joint ALMA Observatory is operated by ESO, AUI/NRAO, and NAOJ. The National Radio Astronomy Observatory is a facility of the National Science Foundation operated under cooperative agreement by Associated Universities, Inc. R.S.'s contribution to the research described here was carried out at JPL, California Institute of Technology, under a contract with NASA. W.V. acknowledges support from ERC consolidator grant 614264.

Appendix

A.1. Analytic Formulation for CO J = 1–0 Optical Depth in an Ultra-Cold Outflow

Using the formulation of Morris (1975), we derive the radiative-contact length, $\delta z\,(p,\, v_p)$, which is the distance along any line of sight (at a given impact parameter, p, relative to the center of the ultra-cold outflow), over which molecules are in radiative contact for a given line-width (due to microtubulence and thermal-broadening), ΔV. Thus,

$$\delta z = \Delta V/(dv_p/dz). \tag{4}$$

Assuming a linearly increasing expansion velocity,

$$V_r = V_0(r/R_0), \tag{5}$$

we find

$$\delta z = R_0(\Delta V/V_0). \tag{6}$$

The opacity per unit length, for a line between rotational energy levels J and $J = 1$, is a product of an absorption coefficient, $\alpha_{J+1,J}\,(r)$, the fractional abundance of the molecule, $f_{\rm mol}$, and the total particle density, $N(r)$. Hence the optical depth is

$$\tau_{J+1,J} = \alpha_{J+1,J}\,(r) f_{\rm mol}\, N\,(r)\delta z. \tag{7}$$

Since

$$\alpha_{J+1,J}\,(r) = \frac{8\,\pi^3\,{\mu_0}^2}{3\,h\,\Delta V}(J\,+\,1)(n_J\,-\,n_{J+1}), \tag{8}$$

then using

$$N\,(r) = \frac{\dot{M}\,(r)}{4\,\pi\,m_{H_2}\,r^2\,V\,(r)}, \tag{9}$$

and assuming a mass-loss rate that varies with the outflow velocity as

$$\dot{M}(r) = \dot{M}_0 [V(r)/V_0]^a, \tag{10}$$

we get

$$\tau_{J+1,J} = \left(\frac{8\,\pi^3\,{\mu_0}^2\,f_{\rm mol}}{3\,h\,V_0}\right)\left(\frac{\dot{M}_0}{4\,\pi\,m_{H_2}\,V_0}\right) \times (J+1)(n_J - n_{J+1})(R_0/r)^{2-a}/r. \tag{11}$$

Setting $T_{\rm exc}(1\text{–}0) < T_{bb}$ ($T_{bb} = 2.725$ K, the microwave background temperature), $n_1 = n_0 \exp\frac{-5.53\,K}{T_{exc}(1-0)}$, hence $n_1 \ll n_0$, and $n_0 = 1$, (i.e., virtually all of the CO population is in the $J = 0$ level), and $\tau_{1,0}$ is independent of $T_{\rm exc}$, i.e.,

$$\tau_{1,0} = \left(\frac{8\,\pi^3\,{\mu_0}^2\,f_{\rm mol}}{3\,h\,V_0}\right)\left(\frac{\dot{M}_0}{4\,\pi\,m_{H_2}\,V_0}\right)(R_0/r)^{2-a} n_0/r. \tag{12}$$

The total mass of the ultra-cold outflow is given by

$$M_{\rm cold} = \frac{\dot{M}_0\,R_0}{V_0}\ln(r_{\rm ou}/r_{\rm in}), \quad a = 0, \tag{13}$$

and

$$M_{\rm cold} = \frac{\dot{M}_0\,R_0}{a\,V_0}\,[(r_{\rm ou}/R_0)^a - (r_{\rm in}/R_0)^a], \quad a \neq 0, \tag{14}$$

where $r_{\rm ou}$ ($r_{\rm in}$) is the outer (inner) radius of the ultra-cold outflow. The kinetic energy in the ultra-cold outflow is

$$KE_{\rm cold} = \frac{\dot{M}_0\,R_0\,V_0}{2a+4}\,[1 - (r_{\rm in}/r_{\rm ou})^{a+2}], \tag{15}$$

A.2. Common-envelope Ejection and Binding Energy

We re-estimate the final binary separation, $2\,a_f$, accounting for the binding and thermal energy of the envelope, i.e.,

$$E_{\rm CEE} = |E_{\rm bind}| - \Delta E_{\rm therm} - \Delta E_{\rm other} + KE_{\rm cold}. \tag{16}$$

We estimate $E_{\rm bind}$ using Equation (13) of De Marco et al. (2011; hereafter DeMetal11),

$$E_{\rm bind} = -G\,M_e(M_e/2 + M_{1,c})/(\lambda\,R), \tag{17}$$

where λ is a parameter with a value of the order of unity,[14] R is the radius of the primary's Roche lobe at the start of the interaction, and M_e is the mass of ejected envelope (which we assume to be equal to the mass of the ultra-cold outflow). The thermal energy term, $\Delta E_{\rm therm}$ is half the value of $E_{\rm bind}$, but with the opposite sign (DeMetal11). We ignore the very uncertain term, $\Delta E_{\rm other}$, which includes contributions from recombination, nuclear fusion, and accretion. The recombination contribution is about $E_{rec} \sim (1.5\text{–}3) \times 10^{46}$ erg for an RGB star of mass $1.6\,M_\odot$ (see tabulated values of E_{rec} in Tables 1 and 2 in Ivanova et al. 2015) and would be larger for the more massive progenitor of the Boomerang.

As before, we take $M_{1,c} = 0.6\ M_\odot$, and $M_e = M_{\rm cold} = 3.3\ M_\odot$. From Table 2 of DeMetal11, we find $\lambda \sim 0.22 - 0.12$ if the primary is on the RGB, and $\lambda \sim 0.33\text{–}0.39$ if it is on the AGB, for $M_1 = 3\text{–}5\ M_\odot$. We take $R \sim 100\ R_\odot$ for a post-RGB object (Table 3 of DeMetal11) and $R \sim 200\ R_\odot$ for a post-AGB object (Equation (20) of DeMetal11, with $M_1 = 4\ M_\odot$).

Hence, for a post-RGB (post-AGB) object, $|E_{\rm bind}| - \Delta E_{\rm therm} \sim (0.64\text{–}1.2) \times 10^{48}$ ($\sim$(0.18–0.21) $\times 10^{48}$) erg, and $E_{\rm CEE} \sim (1.1 - 1.6) \times 10^{48}$ ($\sim$(0.66–0.69) $\times 10^{48}$) erg. Using Equation (2) for $E_{\rm CEE}$, we find that since $a_f \ll a_i$, $\eta \sim 1$, and $2\,a_f \sim 1.4\text{–}2.0(3.3\text{–}3.4)\ R_\odot$ for a post-RGB (post-AGB) object. We note that (i) $M_{\rm cold} = 3.3\ M_\odot$ is the minimum value of the ejected mass; for larger values, a_f will be smaller, and (ii) depending on the relative contribution of $\Delta E_{\rm other}$ to the RHS in Equation (16) above, the value of a_f will be larger.

References

Balick, B., & Frank, A. 2002, ARA&A, 40, 439
Bujarrabal, V., Alcolea, J., Soria-Ruiz, R., et al. 2012, A&A, 537, A8
Bujarrabal, V., Alcolea, J., Van Winckel, H., Santander-García, M., & Castro-Carrizo, A. 2013, A&A, 557, A104
Bujarrabal, V., Castro-Carrizo, A., Alcolea, J., et al. 2016, A&A, 593, A92
Bujarrabal, V., Castro-Carrizo, A., Alcolea, J., et al. 2017, A&A, 597, L5
Canovas, H., Ménard, F., de Boer, J., et al. 2015, A&A, 582, L7
Cracraft, M., & Sparks, W. B. 2007, Instrument Science Report ACS 2007–10 (Baltimore, MD: STSci)
De Marco, O., Passy, J.-C., Moe, M., et al. 2011, MNRAS, 411, 2277
de Ruyter, S., van Winckel, H., Maas, T., et al. 2006, A&A, 448, 641
Draine, B. T., & Hensley, B. 2012, ApJ, 757, 103
Draine, B. T., & Hensley, B. 2013, ApJ, 765, 159
Draine, B. T., & Lazarian, A. 1998, ApJ, 508, 157
Gesicki, K., & Zijlstra, A. A. 2007, A&A, 467, L29
Groenewegen, M. A. T. 2012, A&A, 540, A32

[14] See Ivanova et al. (2013) for a detailed discussion of this parameter.

Herman, J., Burger, J. H., & Penninx, W. H. 1986, A&A, 167, 247
Hony, S., Waters, L. B. F. M., & Tielens, A. G. G. M. 2002, A&A, 390, 533
Huggins, P. J. 2007, ApJ, 663, 342
Huggins, P. J. 2012, in IAU Symp. 283, Planetary Nebulae, ed. A. Manchado, L. Stanghellini, & D. Schönberner (Cambridge: Cambridge Univ. Press), 188
Iaconi, R., Reichardt, T., Staff, J., et al. 2017, MNRAS, 464, 4028
Ivanova, N., Justham, S., Chen, X., et al. 2013, A&ARv, 21, 59
Ivanova, N., Justham, S., & Podsiadlowski, P. 2015, MNRAS, 447, 2181
Jura, M. 1975, AJ, 80, 227
Kamath, D., Wood, P. R., Van Winckel, H., & Nie, J. D. 2016, A&A, 586, L5
Mie, G. 1908, AnP, 330, 377
Miller Bertolami, M. M. 2016, A&A, 588, A25
Morris, M. 1975, ApJ, 197, 603
Pollack, J. B., et al. 1994, ApJ, 421, 615
Sahai, R., Bujarrabal, V., & Zijlstra, A. 1999, ApJL, 518, L115
Sahai, R., Claussen, M. J., Schnee, S., et al. 2011, ApJL, 739, L3
Sahai, R., Morris, M., Sánchez Contreras, C., & Claussen, M. 2007, AJ, 134, 2200
Sahai, R., Morris, M. R., & Villar, G. G. 2011, AJ, 141, 134
Sahai, R., & Nyman, L-Å. 1997, ApJL, 487, L155 (SN97)
Sahai, R., Vlemmings, W., & Nyman, L.-Å. 2015, in ASP Conf. Ser. 499, Revolution in Astronomy with ALMA: The Third Year, ed. D. Iono et al. (San Francisco, CA: ASP), 327
Sahai, R., Vlemmings, W. H. T., Gledhill, T., et al. 2017, ApJL, 835, L13
Sahai, R., Vlemmings, W. H. T., Huggins, P. J., Nyman, L.-Å., & Gonidakis, I. 2013, ApJ, 777, 92
Sahai, R., Wootten, A., Schwarz, H. E., & Wild, W. 1994, ApJ, 428, 237
Silsbee, K., Ali-Haïmoud, Y., & Hirata, C. M. 2011, MNRAS, 411, 2750
Van der Tak, F. F. S., Black, J. H., Schoier, F. L., Jansen, D. J., & van Dishoeck, E. F. 2007, A&A, 468, 627
van Winckel, H., Lloyd Evans, T., Briquet, M., et al. 2009, A&A, 505, 1221
Vassiliadis, E., & Wood, P. R. 1994, ApJS, 92, 125
Wegner, G., & Glass, I. S. 1979, MNRAS, 188, 327
Winters, J. M., Le Bertre, T., Jeong, K. S., Helling, C., & Sedlmayr, E. 2000, A&A, 361, 641
Woitke, P. 2006, A&A, 460, L9
Woodward, C. E., Jones, T. J., Brown, B., et al. 2011, AJ, 141, 181